RSC Advances

PAPER

View Article Online
View Journal | View Issue

Cite this: *RSC Adv.*, 2017, **7**, 9958

Charge storage mechanisms of electrospun Mn_3O_4 nanofibres for high-performance supercapacitors†

Phansiri Suktha,[ab] Nutthaphon Phattharasupakun,[a] Peerapan Dittanet[b] and Montree Sawangphruk*[a]

Mixed oxidation states of manganese oxides are widely used as the electrodes in supercapacitors due to their high theoretical pseudocapacitances. However, their charge storage mechanisms are not yet fully understood. In this work, the charge storage mechanism of Mn_3O_4 or $Mn^{2+}(Mn^{3+})_2O_4$ nanofibres was investigated using a synchrotron-based X-ray absorption spectroscopy (XAS) technique and an *in situ* electrochemical quartz crystal microbalance (EQCM). The average oxidation state of the Mn in the as-synthesized Mn_3O_4 is +2.67. After the first charge, the average oxidation states of Mn at the positive and negative electrodes are +2.61 and +2.38, respectively. The significant change in the oxidation state of Mn at the negative electrode is due to phase transformation of Mn_3O_4 to $Na_\delta MnO_x{\cdot}nH_2O$. Meanwhile, the charge storage mechanism at the positive electrode mainly involves the adsorption of counter ions or solvated SO_4^{2-}. After the first discharge, the calculated Mn average oxidation numbers are +2.51 and +2.53 at the positive and negative electrodes, respectively. At the negative electrode, the solvated Na^+ is desorbed from the electrode surface. At the same time, the solvated SO_4^{2-} is desorbed from the positive electrode. The mass change of solvated Na^+ during charging/discharging is *ca.* 80 ng per cm^2 of the Mn_3O_4 electrode. A symmetric supercapacitor constructed from Mn_3O_4 nanofibres in 0.5 M Na_2SO_4 provides a working potential of 1.8 V, a specific energy of 37.4 W h kg^{-1} and a maximum specific power of 11.1 kW kg^{-1} with 98% capacity retention over 4500 cycles. The understanding of the charge storage mechanism of the mixed oxidation states of $Mn^{2+}(Mn^{3+})_2O_4$ presented in this work could lead to further development of metal oxide-based pseudocapacitors.

Received 20th December 2016
Accepted 26th January 2017

DOI: 10.1039/c6ra28499j

rsc.li/rsc-advances

Introduction

Supercapacitors have higher specific power (2–10 kW kg^{-1})[1] than batteries (0.5–1 kW kg^{-1})[1] and higher specific energy (5–10 W h kg^{-1})[2] than conventional capacitors (0.01–0.05 W h kg^{-1}).[3] Their charge storage mechanisms are based on two phenomena, namely electrochemical double layer capacitance (EDLC) or physisorption of solvated ions on the supercapacitor electrodes, and pseudocapacitance or surface redox reactions. Carbon-based materials, *e.g.* activated carbon, carbon aerogel, graphene, carbon nanotubes and carbon onions, are extensively used as the electrode materials of electrochemical double layer capacitors.[2,4–6] On the other hand, transition metal oxides, *e.g.* RuO_2, NiO, Co_3O_4, MnO_2 and Mn_3O_4, are widely used as active materials for pseudocapacitor electrodes.[7–12] Among all metal oxides, manganese oxides are widely employed as pseudocapacitor electrodes because of their relatively low cost, low toxicity, high theoretical capacitance,[13] and environmental compatibility.[14] A number of manganese oxide structures including MnO, Mn_3O_4, Mn_2O_3, and MnO_2 have been used for high-performance supercapacitors.[13,15–17]

Among all structures, Mn_3O_4 with a normal spinel structure with Mn^{2+} in tetrahedral units and Mn^{3+} in octahedral units[18] with a formula structure of $Mn^{2+}(Mn^{3+})_2O_4$ (ref. 19) provides high pseudocapacitance. Previously, Mn_3O_4-anchored graphene sheets produced by a microwave hydrothermal method have exhibited a specific capacitance (SC) of 70 F g^{-1} at 0.2 A g^{-1} in 1 M Na_2SO_4.[20] A graphene-supported Mn_3O_4 nanocomposite synthesized by a precipitation method gives a SC of 61 F g^{-1} at 0.1 A g^{-1} in 1 M K_2SO_4.[21] Mn_3O_4 nanoparticles (NPs) prepared by ultrasonication and hydrolysation provide a SC of 261 F g^{-1} at 0.4 A g^{-1} in 1 M Na_2SO_4 (ref. 22) and those produced by chemical precipitation show a SC of 322 F g^{-1} at 0.5 mA cm^{-2} in 1 M Na_2SO_4.[23] More interestingly, 1D nanofibres of mixed Mn_2O_3 and Mn_3O_4 produced by an electrospinning process, which is a simple, efficient, and reproducible method,[24] exhibit a SC of

[a]*Department of Chemical and Biomolecular Engineering, School of Energy Science and Engineering, Vidyasirimedhi Institute of Science and Technology, Rayong 21210, Thailand. E-mail: montree.s@vistec.ac.th*

[b]*The Center of Excellence on Petrochemical and Materials Technology, Department of Chemical Engineering, Faculty of Engineering, NANOTEC Center for Nanoscale Materials Design for Green Nanotechnology, Center for Advanced Studies in Nanotechnology and its Applications in Chemical, Food and Agricultural Industries, Kasetsart University, Thailand*

† Electronic supplementary information (ESI) available. See DOI: 10.1039/c6ra28499j

360.7 F g^{-1} at 1 A g^{-1} in 0.5 M Na_2SO_4.[25] This indicates that 1D nanofibres can enhance both the ion transport pathways and the surface area, increasing the contact area between the electrolyte ions and the surface of the electrodes.[25] The porosity of the nanofibers also plays an important role in the charge storage performance of the supercapacitors.[26,27] Micropores can help increase the electrochemical double layer capacitance due to their high surface area, while mesopores can enhance electrolyte ion transportation. For example, MnO_x nanofibers with a pore size of around 10–30 nm provide very good electrolyte diffusion.[28]

However, the charge storage mechanism of Mn_3O_4 is unclear and rather complex.[8,29,30] In this work, we have investigated the charge storage mechanism of Mn_3O_4 nanofibres using high-resolution synchrotron-based X-ray absorption (XAS) and electrochemical quartz crystal microbalance (EQCM) techniques. The results here showed that Mn_3O_4 nanofibres produced by an electrospinning process using 10 wt% manganese acetate ($Mn(OAc)_2$) in polyacrylonitrile (PAN) solution provide higher SCs than other samples. The charge storage mechanism of the Mn_3O_4 nanofibres investigated by XAS involves a phase transformation of Mn_3O_4 to $Na_\delta MnO_x \cdot nH_2O$ during the first charge. Subsequently, the mechanism is based on surface redox reactions. The mass change of solvated Na^+ during charging/discharging is *ca.* 80 ng per cm^2 of the Mn_3O_4 electrode.

Experimental section

Electrospinning of manganese oxide nanofibres

Firstly, 1 g of PAN (M_w = 150 000, Aldrich) was dissolved in 10 ml of dimethylformamide (DMF) (Qrec, 99.8%) at 60 °C under stirring and then cooled down to room temperature. Then, 0.052 g of manganese acetate tetrahydrate ($Mn(OAc_2)\cdot 4H_2O$) (Acros, 99+%) was added into the PAN solution. The PAN/$Mn(OAc_2)$ solution was subsequently put into a syringe, and the distance between the syringe tip and an aluminium foil collector was fixed at 10 cm. The electrospinning process was subsequently operated at a feed flow rate of 2 ml h^{-1} and the applied potential was finely tuned to 15 kV. The $Mn(OAc_2)$ content (0.11 g for 10 wt%, 0.25 g for 20 wt%, 0.42 g for 30 wt%, and 0.56 g for 36 wt%) was also varied to finely tune the homogeneous electrospun nanofibres. Finally, the as-spun nanofibres were dried at ambient temperature for 24 h and calcined at 500 °C with a heating rate of 5 °C min^{-1} for 2 h.

Characterization of the electrospun nanofibres

The morphologies of the as-electrospun nanofibres and as-calcined manganese oxide nanofibres were characterized by SEM-EDX (SEM-EDX, Philips XL30) and TEM (TEM, Hitachi HT7700). The crystalline structure of the as-calcined nanofibres was characterized by XRD (XRD PHILIPS, X'Pert-MPD 40 kV 35 mA, Cu Kα 1.54056 Å) with a 2θ range of 10–80° and a step size of 0.02° s^{-1}. The electronic structure of the nanofibres was characterized by X-ray absorption spectroscopy (XAS), at the Synchrotron Light Research Institute (Thai Public Organization). More details on the XAS measurement procedures can be found in our previous report.[31]

Electrochemical characterization

The electrochemical properties of the nanofibres were tested by cyclic voltammetry (CV), galvanostatic charge/discharge (GCD), and electrochemical impedance spectroscopy (EIS) in 0.5 M Na_2SO_4 electrolyte using a Metrohm AUTOLAB potentiostat (PGSTAT 302N). Platinum wire and Ag/AgCl (3 M KCl) were used as a counter electrode and a reference electrode, respectively. In a two-electrode system, GCD was measured using a NEWARE battery tester (GELON LIB., CTS 20V-5A-GGS). The as-calcined MnO_x nanofibres were mixed with a conductive additive (carbon black, CB) and an adhesive binder (polyvinylidene fluoride, PVDF) at a weight ratio of 6 : 3 : 1 (MnO_x : CB : PVDF) in *N*-methyl-2-pyrrolidone (NMP). The mixture was then spray-coated onto functionalized-carbon fibre paper with dimensions of 1 × 1 cm^2 for the three-electrode system and a circle with a diameter of 1.58 cm for the two-electrode system. The mass loading was about 2 mg cm^{-2} for each electrode. The electrode was dried at 80 °C for 24 h. The hydrolysed polyethylene (PE) separator was soaked in 0.5 M Na_2SO_4 and inserted between the two working electrodes in a coin case (2016 type). Finally, the symmetric supercapacitor device was fabricated using a hydraulic compression machine at 800 psi. The *in situ* charge storage mechanism of the MnO_x nanofibre electrodes was characterized using an electrochemical quartz crystal microbalance (EQCM) with Ag/AgCl (3 M KCl) gel as the reference electrode, Au wire as the counter electrode, and about 0.6–0.7 mg cm^{-2} of the sample coated on an Au support (0.67 cm in diameter).

Results and discussion

The morphologies of the as-electrospun PAN/$Mn(OAc)_2$ nanofibres with different $Mn(OAc)_2$ contents in PAN are shown in Fig. 1. The diameters of the as-electrospun nanofibres are about 400–500, 430–500, 500–600, 900–1800, and 900–1700 nm for 5, 10, 20, 30 and 36 wt% $Mn(OAc)_2$, respectively.

Fig. 2 shows the morphology of the MnO_x nanofibres after calcining at 500 °C for 2 h. After the removal of PAN, the diameter of the as-calcined MnO_x nanofibres is reduced. With increasing $Mn(OAc)_2$ concentrations, the as-calcined MnO_x formed larger nanofibres. The diameters of the MnO_x nanofibres are 60–125, 60–200, 150–250, 300–600, and 300–600 nm for 5, 10, 20, 30 and 36 wt% $Mn(OAc)_2$, respectively. The presence of Mn and O in the as-obtained nanofibres was confirmed by EDX (Fig. 2f). In addition, it is clearly seen from the TEM images that the MnO_x nanofibres are formed from connected MnO_x particles with open pores in the structure. Note that the PAN/$Mn(OAc)_2$ fibres with rather large diameters cannot be dispersed in solvents and so are not suitable for TEM measurements.

Fig. 3 shows the XRD patterns of the as-calcined MnO_x nanofibres. The XRD patterns of the MnO_x produced using 5–20 wt% $Mn(OAc)_2$ are assigned to Mn_3O_4 (JCPDS 24-0734).[25] In addition, the XRD patterns of the MnO_x prepared using 30 and 36 wt% $Mn(OAc)_2$ show mixed crystalline phases of Mn_3O_4 and Mn_2O_3 (JCPDS 073-1826).[25] The Mn_3O_4 and Mn_2O_3 crystallite

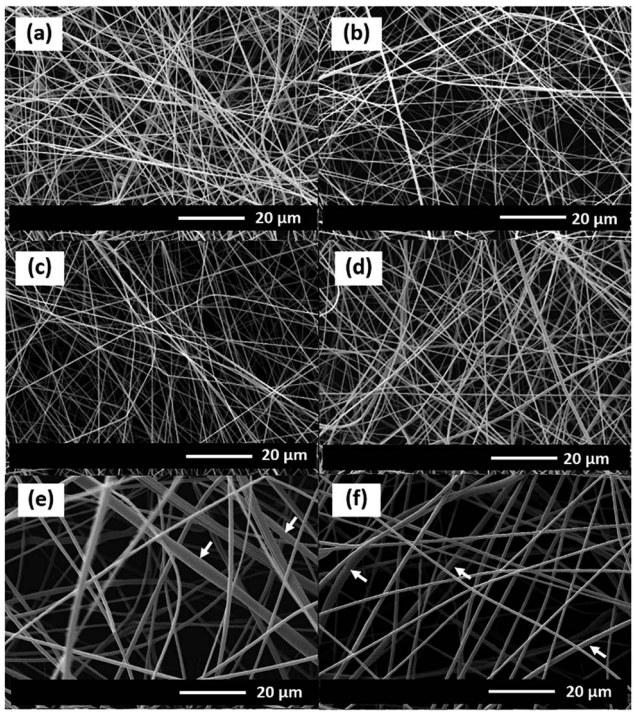

Fig. 1 SEM images of the as-electrospun PAN nanofibres at different $Mn(OAc)_2$ loading contents: (a) 0, (b) 5, (c) 10, (d) 20, (e) 30, and (f) 36 wt%.

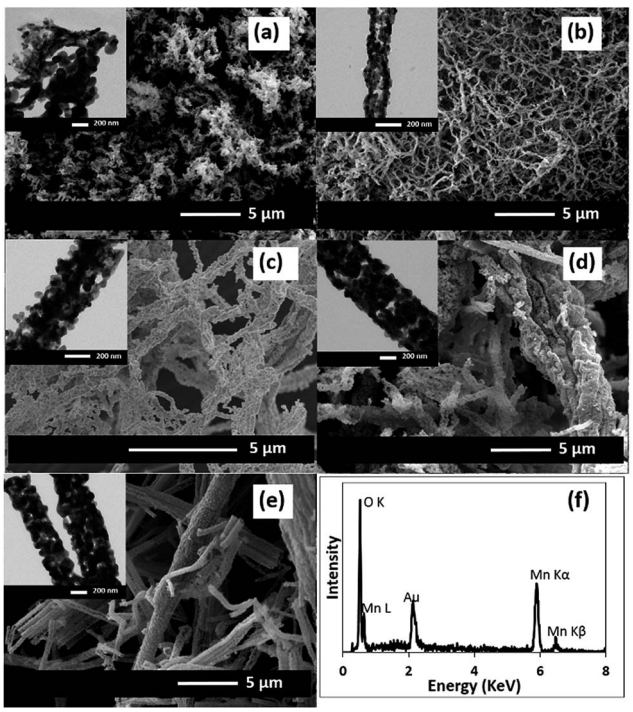

Fig. 2 SEM and TEM images of the MnO_x nanofibres formed with different $Mn(OAc)_2$ concentrations after calcining at 500 °C: (a) 5, (b) 10, (c) 20, (d) 30, and (e) 36 wt%. (f) The EDX spectrum of the MnO_x nanofibres produced using 36 wt% $Mn(OAc)_2$.

sizes are estimated using Scherrer's equation from the (211) and (222) planes, respectively. The Mn_3O_4 crystallite sizes are 13.3, 30.7, 42.3, 35.4 and 36.9 nm at 5, 10, 20, 30 and 36 wt%

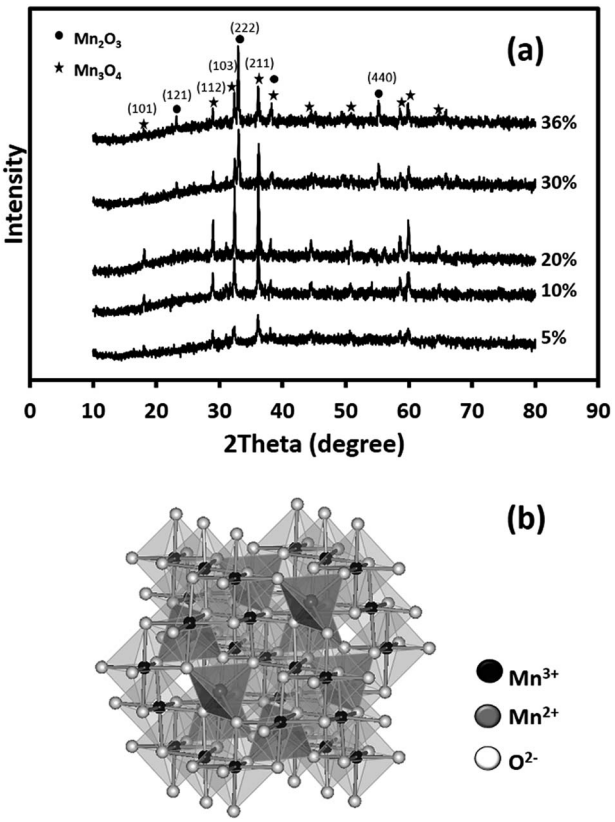

Fig. 3 (a) XRD patterns of the as-calcined MnO_x nanofibres electrospun at different $Mn(OAc)_2$ loading contents at 15 kV and (b) a crystal structure model of spinel Mn_3O_4.

$Mn(OAc)_2$, respectively. Meanwhile, the Mn_2O_3 crystallite sizes are 30.5 and 30.9 nm at 30 and 36 wt% $Mn(OAc)_2$, respectively. Note that the Mn_2O_3 phase is easily removed by calcination at high temperature (see Fig. S1†). The formation of Mn_3O_4 occurs *via* reactions (1) and (2):[24]

$$Mn(CH_3COO)_2 \cdot 4H_2O \rightarrow Mn(OH)(CH_3COO) + 3H_2O + CH_3COOH \quad (1)$$

$$3Mn(OH)(CH_3COO) \rightarrow Mn_3O_4 + 2CO_2 + CO + 3CH_4 \quad (2)$$

Intermediate reactions are proposed as shown in reactions (3) and (4):[32]

$$2Mn(OH)(CH_3COO) \rightarrow Mn_2O_3 + CO_2 + CO + 2CH_4 \quad (3)$$

$$6Mn_2O_3 \rightarrow 4Mn_3O_4 + O_2 \quad (4)$$

Fig. 4 shows the electrochemical properties of the as-calcined MnO_x nanofibres produced using different $Mn(OAc)_2$ contents. From the CV curves (Fig. 4a), the Mn_3O_4 nanofibres electrospun at 10 wt% $Mn(OAc)_2$ exhibit the largest area under the curve, leading to the highest capacitance. The SCs of the symmetric Mn_3O_4 nanofibre supercapacitor at scan rates of 10, 20, 50, 70, and 100 mV s^{-1} are 161, 154, 130, 115, and 98 F g^{-1}, respectively. The GCD result in Fig. 4b is in good agreement

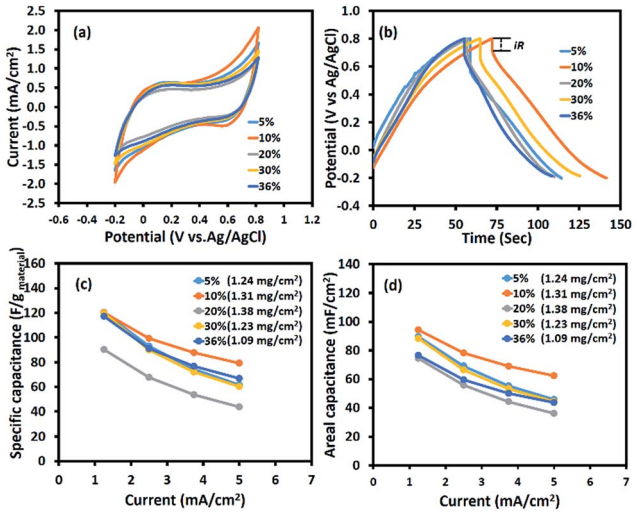

Fig. 4 (a) Cyclic voltammograms at a scan rate of 10 mV s^{-1}, (b) galvanostatic charge–discharge curves at 1.25 mA cm^{-2}, (c) the specific capacitance *vs.* applied current, and (d) the areal capacitances *vs.* applied current of the half-cell Mn_3O_4 electrodes in 0.5 M Na_2SO_4 electrolyte.

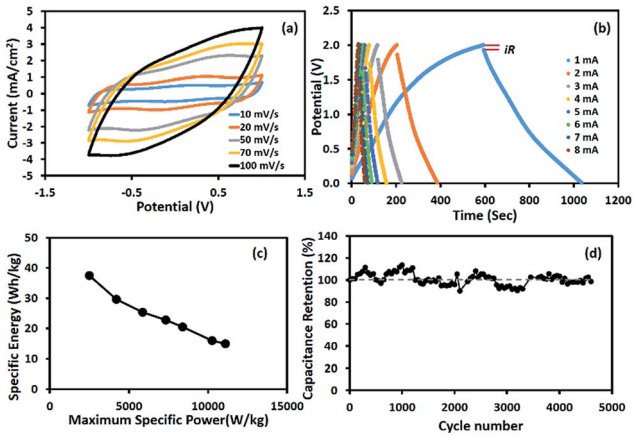

Fig. 5 (a) CV curves, (b) GCD curves, (c) Ragone plot, and (d) capacity retention of the symmetric supercapacitor based on Mn_3O_4 nanofibres electrospun at 10 wt% $Mn(OAc)_2$ in 0.5 M Na_2SO_4.

with the CV result. The working potential of the electrode excluding *iR* drop is *ca.* 0.9 V *vs.* Ag/AgCl. The Mn_3O_4 nanofibres produced with 10 wt% $Mn(OAc)_2$ content exhibit the highest capacitance because of their high surface area and 3D porous structure, which enhances the contact area between the electrode and the electrolyte,[25] and their small crystallite size, which can enhance charge transport.[33] Meanwhile, the Mn_3O_4 nanofibres electrospun at 20 wt% $Mn(OAc)_2$ show the lowest capacitance due to large crystallite size, which leads to poor charge transport. As the conductivity of Mn_3O_4 is relatively higher than that of Mn_2O_3,[25] the Mn_3O_4 nanofibres produced at 10 wt% $Mn(OAc)_2$ provide a higher SC than the mixed Mn_3O_4 and Mn_2O_3 nanofibres electrospun at 30–36 wt% $Mn(OAc)_2$. The specific and areal capacitances of the Mn_3O_4 electrodes at different applied currents in 0.5 M Na_2SO_4 are shown in Fig. 4c and d, respectively. The charge storage performance of the Mn_3O_4 electrodes is under the diffusion limit since their capacitances decrease with increasing applied currents.

The charge storage performance of the symmetric supercapacitor based on the Mn_3O_4 nanofibres produced at 10 wt% $Mn(OAc)_2$ is shown in Fig. 5. The cyclic voltammograms in Fig. 5a show pseudocapacitive behaviour with a broad peak due to surface redox reactions. The GCD curves in Fig. 5b show a wide working potential of 1.8 V excluding *iR* drop, which is twice that of the half-cell electrode. The calculated capacitances decrease with increasing scan rates and applied currents due to the limited diffusion of solvated ions.[34] The calculated SC is 289 F g^{-1} at 1 mA for each cell or 1.25 mA cm^{-2}. Table 1 compares the charge storage performances of Mn_3O_4-based supercapacitors. Most previous reports were based on a three-electrode system or half-cell.

The Ragone plot of the device is shown in Fig. 5c. The specific energy and maximum specific power of the Mn_3O_4 symmetric supercapacitor are 37.4 W h kg^{-1} and 11.1 kW kg^{-1}, respectively (see the calculation details in the ESI†). The stability of the symmetric supercapacitor based on the as-electrospun Mn_3O_4 nanofibres is shown in Fig. 5d, for which the capacity retention is over 98% after 4500 charge/discharge cycles.

To further investigate the charge storage mechanism of Mn_3O_4, the average oxidation number of Mn at the positive and negative electrodes of the device after the 1st charge, the 1st discharge, and the long-term stability test of over 4500 cycles was determined by XAS. The normalized X-ray absorption near edge spectra (XANES) of the Mn-based materials are shown in Fig. 6a–c. The K-edge electron binding energies of Mn metal, MnO, Mn_2O_3, and Mn_3O_4 standards are 6539.00, 6544.17, 6548.61, and 6547.15 eV, respectively. After the 1st charge, the

Table 1 Charge storage performances of Mn_3O_4-based supercapacitor electrodes

Materials	Tested method	Electrolyte	Specific capacitance	Ref.
Mn_3O_4 nanoparticles	GCD at 0.1 A g^{-1}	1 M Na_2SO_4	85 F g^{-1} (three electrodes)	35
Mn_3O_4 stacked sheet	CV at 10 mV s^{-1}	H_2SO_4–PVA (1 : 1 wt) gel electrolyte	127 F g^{-1} (two electrodes)	36
Mn_3O_4 nanoparticles	GCD at 0.5 mA cm^{-2}	1 M Na_2SO_4	322 F g^{-1} (three electrodes)	23
Mn_3O_4 nanoparticles	GCD at 0.5 mA cm^{-2}	1 M Na_2SO_4	113 F g^{-1} (three electrodes)	7
As-spun Mn_3O_4 fibres	GCD at 0.3 A g^{-1}	1 M Na_2SO_4	155 F g^{-1} (three electrodes)	28
As-spun MnO_x fibres	CV at 10 mV s^{-1}	1 M Na_2SO_4	161.22 F g^{-1} (two electrodes)	37
As-spun Mn_3O_4 fibres	CV at 2 mV s^{-1}	0.5 M Na_2SO_4	63.2 F g^{-1} (three electrodes)	38
As-spun Mn_3O_4 nanofibres	GCD at 1 mA (1.25 mA cm^{-2})	0.5 M Na_2SO_4	289 F g^{-1} (two electrodes)	This work

K-edge electron binding energies of Mn at the positive and negative electrodes were in between those of MnO (Mn^{2+}) and Mn_2O_3 (Mn^{3+}) at 6547.60 and 6546.80 eV, respectively. The average oxidation numbers of Mn at the positive and negative electrodes calculated using eqn (S8) in the ESI†[39] are 2.61 and 2.38, respectively. Note that the average oxidation state of Mn in the as-calcined Mn_3O_4 is +2.67 (see Fig. 6d). The decreased oxidation number of Mn, especially at the negative electrode after the 1st charge, when compared with the bare electrode is due to solvated Na^+ being inserted into the structure. The charge storage mechanism follows reactions (5) and (6):

$$Mn_3O_4 \xrightarrow{1st\ charge} Na_\delta MnO_x \cdot nH_2O \quad (5)$$

$$Na_\delta MnO_x \cdot nH_2O \leftrightarrow MnO_x \cdot nH_2O + \delta Na^+ + \delta e^- \quad (6)$$

This is because the adsorption of solvated cations can result in a lower binding energy.[8,40] On the other hand, the partial oxidation of Mn^{2+} to Mn^{3+} at the positive electrode after the 1st charge leads to a slight change in the average oxidation number of Mn. Meanwhile, reduction of Mn^{3+} to Mn^{2+} occurs at the negative electrode, which significantly reduces the average oxidation number of Mn.

After the 1st discharge, the K-edge electron binding energies of Mn at the positive and negative electrode are 6547.58 and 6547.39 eV, respectively. The calculated Mn average oxidation numbers are +2.51 and +2.53 at the positive and negative electrodes, respectively. At the negative electrode, the solvated Na^+ is desorbed from the electrode surface. At the same time, solvated SO_4^{2-} is desorbed from the positive electrode. After the stability test, the average oxidation numbers of Mn at the positive and negative electrodes are +2.43 and +2.38, respectively, calculated from the K-edge electron binding energies of 6546.77 eV and 6546.69 eV, respectively. This decrease is due to the extraction of Mn^{2+} from the crystal structure. Note that all of the binding energies and oxidation states of Mn are listed in Table S1 of the ESI.†

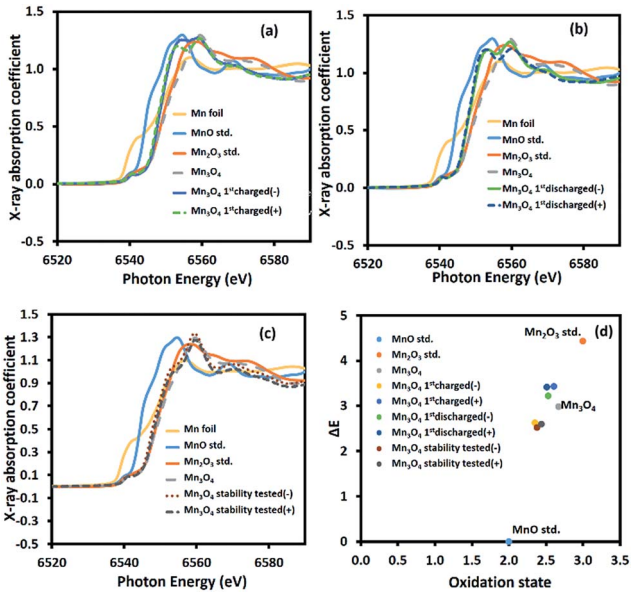

Fig. 6 *Ex situ* high-resolution XAS spectra after (a) the 1st charge, (b) the 1st discharge, and (c) the stability test, and (d) the average oxidation numbers of Mn in the manganese oxide electrodes compared with the Mn standard compounds.

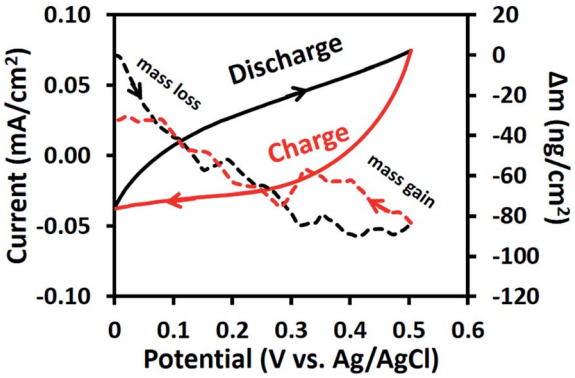

Fig. 7 CV curves and EQCM measurements of the as-electrospun Mn_3O_4 nanofibre electrode in 0.5 M Na_2SO_4.

The EQCM results of the as-electrospun Mn_3O_4 nanofibres in 0.5 M Na_2SO_4 at a scan rate of 10 mV s^{-1} are shown in Fig. 7. For the anodic potentials scanned from 0 to 0.5 V *vs.* Ag/AgCl, the mass change is reduced or under zero due to desorption of solvated Na^+ cations. On the other hand, an augmented mass change is observed for the cathodic potential scanned from 0.5 to 0 V *vs.* Ag/AgCl due to the adsorption of solvated cations.[41] However, the final mass change of the cathodic scan does not meet the initial mass change of the anodic scan. This confirms the XAS results, which showed that the average oxidation state of Mn changes over time or during cycling. In other words, the charge storage mechanism of the as-electrospun Mn_3O_4 nanofibres involves solvated cation adsorption/desorption with a mass change of *ca.* 80 ng cm^{-2}. These EQCM results support the XAS results.

Conclusions

Manganese oxide (Mn_3O_4) nanofibres were prepared by an electrospinning process of $Mn(OAc_2)$ in PAN with a subsequent calcination process at 500 °C for 2 h. The effect of the $Mn(OAc_2)$ loading content was investigated and it was found that the amount of $Mn(OAc_2)$ precursor affected the crystalline structure of the final Mn_3O_4 nanofibre products. The Mn_3O_4 nanofibres produced with different $Mn(OAc_2)$ contents were coated onto flexible CFP substrates using a spray coating technique and then electrochemically evaluated by CV, GCD, and EIS methods. The symmetric supercapacitor based on Mn_3O_4 nanofibres with diameters of 60–200 nm produced at 10 wt% $Mn(OAc_2)$ exhibits the highest SC, specific energy, and maximum specific power of 289 F g^{-1} at 1 mA, 37.4 W h kg^{-1} and 11.1 kW kg^{-1}, respectively. The capacity retention is *ca.* 98% over 4500 cycles. Based on XAS, the charge storage mechanism of the as-calcined Mn_3O_4 nanofibres involves a phase transformation from Mn_3O_4 to

$Na_\delta MnO_x \cdot nH_2O$ during the first charge. After this, the mechanism is based on surface redox reactions due to adsorption/desorption of solvated ions. In addition, the EQCM measurements show that the solvated cation adsorption/desorption with a mass change of *ca.* 80 ng cm^{-2} on the Mn_3O_4 nanofibres plays a significant role in the charge storage mechanism of Mn_3O_4. The understanding of the charge storage mechanism of $Mn^{2+}(Mn^{3+})_2O_4$ presented in this work could lead to further development of metal oxide-based pseudocapacitors.

Acknowledgements

This work was financially supported by the Thailand Research Fund and Vidyasirimedhi Institute of Science and Technology (RSA5880043). P. Suktha thanks the Centre of Excellence on Petrochemical and Materials Technology (PETROMAT), Department of Chemical Engineering, Faculty of Engineering, Kasetsart University, KURDI, the National Research University Project of Thailand (NRU) for financial support.

Notes and references

1 B. Vidyadharan, R. A. Aziz, I. I. Misnon, G. M. Anil Kumar, J. Ismail, M. M. Yusoff and R. Jose, *J. Power Sources*, 2014, **270**, 526–535.
2 P. Iamprasertkun, A. Krittayavathananon and M. Sawangphruk, *Carbon*, 2016, **102**, 455–461.
3 M. Winter and R. J. Brodd, *Chem. Rev.*, 2004, **104**, 4245–4270.
4 J. Chmiola, G. Yushin, Y. Gogotsi, C. Portet, P. Simon and P. L. Taberna, *Science*, 2006, **313**, 1760–1763.
5 P. Huang, C. Lethien, S. Pinaud, K. Brousse, R. Laloo, V. Turq, M. Respaud, A. Demortière, B. Daffos, P. L. Taberna, B. Chaudret, Y. Gogotsi and P. Simon, *Science*, 2016, **351**, 691–695.
6 D. Pech, M. Brunet, H. Durou, P. Huang, V. Mochalin, Y. Gogotsi, P.-L. Taberna and P. Simon, *Nat. Nanotechnol.*, 2010, **5**, 651–654.
7 B. G. S. Raj, R. N. R. Ramprasad, A. M. Asiri, J. J. Wu and S. Anandan, *Electrochim. Acta*, 2015, **156**, 127–137.
8 L. Yang, S. Cheng, X. Ji, Y. Jiang, J. Zhou and M. Liu, *J. Mater. Chem. A*, 2015, **3**, 7338–7344.
9 G. S. Gund, D. P. Dubal, B. H. Patil, S. S. Shinde and C. D. Lokhande, *Electrochim. Acta*, 2013, **92**, 205–215.
10 C.-H. Yang, I. W. Sun, C.-T. Hsieh, T.-Y. Wu, C.-Y. Su, Y.-S. Li and J.-K. Chang, *J. Mater. Chem. A*, 2016, **4**, 4015–4018.
11 M.-J. Deng, P.-J. Ho, C.-Z. Song, S.-A. Chen, J.-F. Lee, J.-M. Chen and K.-T. Lu, *Energy Environ. Sci.*, 2013, **6**, 2178–2185.
12 M.-J. Deng, J.-K. Chang, C.-C. Wang, K.-W. Chen, C.-M. Lin, M.-T. Tang, J.-M. Chen and K.-T. Lu, *Energy Environ. Sci.*, 2011, **4**, 3942–3946.
13 M. Sawangphruk, P. Srimuk, P. Chiochan, A. Krittayavathananon, S. Luanwuthi and J. Limtrakul, *Carbon*, 2013, **60**, 109–116.
14 D. Yang, *J. Power Sources*, 2011, **196**, 8843–8849.
15 S. Chen, F. Liu, Q. Xiang, X. Feng and G. Qiu, *Electrochim. Acta*, 2013, **106**, 360–371.
16 X. Hao, J. Zhao, Y. Li, Y. Zhao, D. Ma and L. Li, *Colloids Surf., A*, 2011, **374**, 42–47.
17 N. Phattharasupakun, J. Wutthiprom, P. Chiochan, P. Suktha, M. Suksomboon, S. Kalasina and M. Sawangphruk, *Chem. Commun.*, 2016, **52**, 2585–2588.
18 D. P. Dubal, D. S. Dhawale, R. R. Salunkhe, S. M. Pawar and C. D. Lokhande, *Appl. Surf. Sci.*, 2010, **256**, 4411–4416.
19 L. Laffont and P. Gibot, *Mater. Charact.*, 2010, **61**, 1268–1273.
20 L. Li, K. H. Seng, H. Liu, I. P. Nevirkovets and Z. Guo, *Electrochim. Acta*, 2013, **87**, 801–808.
21 F. Gao, J. Qu, Z. Zhao, Q. Zhou, B. Li and J. Qiu, *Carbon*, 2014, **80**, 640–650.
22 L. Wang, L. Chen, Y. Li, H. Ji and G. Yang, *Powder Technol.*, 2013, **235**, 76–81.
23 B. Gnana Sundara Raj, A. M. Asiri, J. J. Wu and S. Anandan, *J. Alloys Compd.*, 2015, **636**, 234–240.
24 N. A. Barakat, K.-D. Woo, S. Ansari, J.-A. Ko, M. A. Kanjwal and H. Y. Kim, *Appl. Phys. A: Mater. Sci. Process.*, 2009, **95**, 769–776.
25 E. Lee, T. Lee and B.-S. Kim, *J. Power Sources*, 2014, **255**, 335–340.
26 Z. Li, X. Hu, D. Xiong, B. Li, H. Wang and Q. Li, *Electrochim. Acta*, 2016, **219**, 339–349.
27 J. Zhao, C. Lai, Y. Dai and J. Xie, *Mater. Lett.*, 2007, **61**, 4639–4642.
28 J. Bhagwan, A. Sahoo, K. L. Yadav and Y. Sharma, *Electrochim. Acta*, 2015, **174**, 992–1001.
29 S. Komaba, T. Tsuchikawa, A. Ogata, N. Yabuuchi, D. Nakagawa and M. Tomita, *Electrochim. Acta*, 2012, **59**, 455–463.
30 T.-H. Wu, D. Hesp, V. Dhanak, C. Collins, F. Braga, L. J. Hardwick and C.-C. Hu, *J. Mater. Chem. A*, 2015, **3**, 12786–12795.
31 P. Iamprasertkun, A. Krittayavathananon, A. Seubsai, N. Chanlek, P. Kidkhunthod, W. Sangthong, S. Maensiri, R. Yimnirun, S. Nilmoung, P. Pannopard, S. Ittisanronnachai, K. Kongpatpanich, J. Limtrakul and M. Sawangphruk, *Sci. Rep.*, 2016, **6**, 37560.
32 K. Terayama and M. Ikeda, *Trans. Jpn. Inst. Met.*, 1983, **24**, 754–758.
33 A. González, E. Goikolea, J. A. Barrena and R. Mysyk, *Renewable Sustainable Energy Rev.*, 2016, **58**, 1189–1206.
34 P. Suktha, P. Chiochan, P. Iamprasertkun, J. Wutthiprom, N. Phattharasupakun, M. Suksomboon, T. Kaewsongpol, P. Sirisinudomkit, T. Pettong and M. Sawangphruk, *Electrochim. Acta*, 2015, **176**, 504–513.
35 Y. Fan, X. Zhang, Y. Liu, Q. Cai and J. Zhang, *Mater. Lett.*, 2013, **95**, 153–156.
36 D. P. Dubal and R. Holze, *Energy*, 2013, **51**, 407–412.
37 K. Mondal, C.-Y. Tsai, S. Stout and S. Talapatra, *Mater. Lett.*, 2015, **148**, 142–146.
38 X. Zhao, Y. Du, Y. Li and Q. Zhang, *Ceram. Int.*, 2015, **41**, 7402–7410.
39 S. Daengsakul, P. Kidkhunthod, O. Soisang, T. Kuenoon, A. Bootchanont and S. Maensiri, *Microelectron. Eng.*, 2015, **146**, 38–42.
40 K. P. Lucht and J. L. Mendoza-Cortes, *J. Phys. Chem. C*, 2015, **119**, 22838–22846.
41 W.-Y. Tsai, P.-L. Taberna and P. Simon, *J. Am. Chem. Soc.*, 2014, **136**, 8722–8728.